Supporting Information

Trimodal Operation of a Robust Smart Organic Crystal

Wu et al.

1. Materials and methods

Materials. 4-chlorobenzhydrazide was purchased from Tianjin Xiensi Opd Technology Co., Ltd. 4-(trifluoromethoxy)benzaldehyde was purchased from Shanghai Bide Pharmaceutical Technology Co., Ltd. with purity of > 98% and was used without further purification.

Nuclear magnetic resonance (NMR) spectroscopy. The NMR spectra were recorded on JNM-ECZ400S/L1 400 MHz spectrometer. Deuterated acetone was used as solvent, and tetramethylsilane was used as the internal standard.

Thermal Analysis. DSC measurement was performed on a calorimeter model DSC 1 (Mettler Toledo, Switzerland) calibrated with standard indium and zinc under a nitrogen atmosphere to determine the thermodynamic properties of the samples. Samples weighing 5–10 mg were placed in standard aluminum pans and heated at a heating rate of 10 K min^{-1} under a nitrogen gas flow of 50 mL min^{-1}.

Single-crystal X-ray diffraction. Single crystal X-ray diffraction (SCXRD) measurements were carried out on 007HF XtaLAB P20 (Rigaku, Japan) diffractometer. The data was collected in the range 270–380 K in 10 K-increments, while the temperature was controlled with an Oxford Cryostream 800 Cooler. Olex2 was used to solve the structure by intrinsic phasing methods (SHELXT),[1] and the full-matrix least-squares methods on F^2 (SHELXL) was used to complete and refine the structure models.[2]

Powder X-ray diffraction. The powder X-ray diffraction data were obtained on a Rigaku D/max-2500 (Rigaku, Japan) using Cu K_α radiation (1.5405 Å), with a step size of 0.02° and a scanning rate of 0.067° s^{-1} over the diffraction angle (2θ) range of 5–40°.

Infrared spectroscopy. The Fourier transform infrared (FTIR) spectra were recorded by using a Bruker Alpha FTIR spectrometer with 4 cm^{-1} resolution and 16 scans per spectrum in the 4000–400 cm^{-1} range.

Hot-stage microscopy. The hot-stage microscopic observations were carried out by using a Linkam system which consisted of a temperature-controlled stage LNP94/2 mounted on a microscope CX40P.

Scanning electron microscopy. The morphology of the crystals was observed by using an X650 scanning electron microscope (Hitachi, Japan). The samples were mounted by using a carbon adhesive on an aluminum holder, sputtered with gold, and scanned at a voltage of 15 kV under vacuum.

Nanoindentation. The nanoindentation tests were conducted by using nanomechanical test instrument TI Premier (Hysitron Inc., USA) with a Berkovich diamond tip indenting the main crystal facets. All crystals were firmly affixed on the test stage with a cyanoacrylate glue. Peak load P_{max} = 5 mN at loading/unloading rate of 0.5 mN s^{-1} and hold time of 10 s was applied in all cases. A minimum of 10

indentations were carried on each crystal facet to obtain satisfactory statistics. The *P–h* response curves were analyzed by using the standard Oliver-Pharr method.

Theoretical calculations. The energy frameworks were calculated by using the B3LYP/6-31G (d,p) method and the software CrystalExplorer17.5.[3] The pairwise interaction energies were calculated within a molecule-molecule distance of 3.8 Å. The scale factor of tube size and the energy threshold values for plotting the energy frameworks were set to 200 and 5 kJ mol^{-1}, respectively.

2. Synthesis
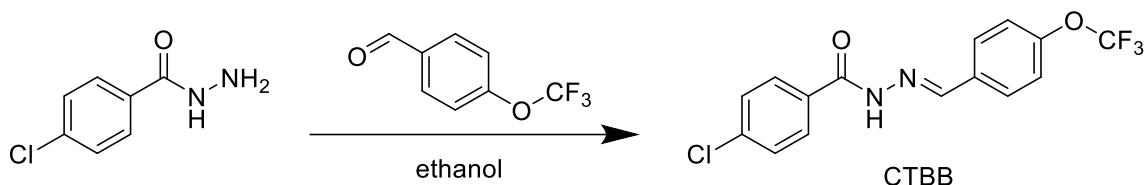
Scheme 1. Synthetic procedure for preparation of the Schiff base (*E*)-4-chloro-*N'*-(4-(trifluoromethoxy)-benzylidene) benzohydrazide (CTBB).

1.71 g (10 mmol) 4-chlorobenzhydrazide and 50 mL of anhydrous ethanol were added to a 100 mL thermostat and stirred to dissolve at 30 °C. 4-(trifluoromethoxy)benzaldehyde (1.46 mL, 10 mmol) was added, and the mixture was stirred at 30 °C for 3 h. After the reaction completed, the product was filtered with cold methanol. The resulting filter cake afforded 3.21 g of orange-red pure solid of (*E*)-4-chloro-*N'*-(4-(trifluoromethoxy)benzylidene)benzohydrazide (yield: 89.1%). ^{1}H NMR (400 MHz, DMSO-d_6) δ 12.01 (s, 1H), 8.47 (s, 1H), 7.90 (dd, J = 32.2, 8.4 Hz, 4H), 7.60 (d, J = 8.3 Hz, 2H), 7.45 (d, J = 8.1 Hz, 2H).

3. Crystal growth

Form I: 1 mL saturated acetone solution of CTBB was placed in a test tube (the concentration was about 2 mol L^{-1}), and then 2 mL of acetone was added along the wall, followed by slow addition of 15 mL *n*-hexane along the walls. The mouth of the test tube was covered with parafilm, and the solution was left to stand 5–7 days. Colorless needle-like crystals were obtained. **Form II:** Form II was obtained by heating form I to 380 K. **Form III:** Form III was obtained by sublimation form I at 383 K.
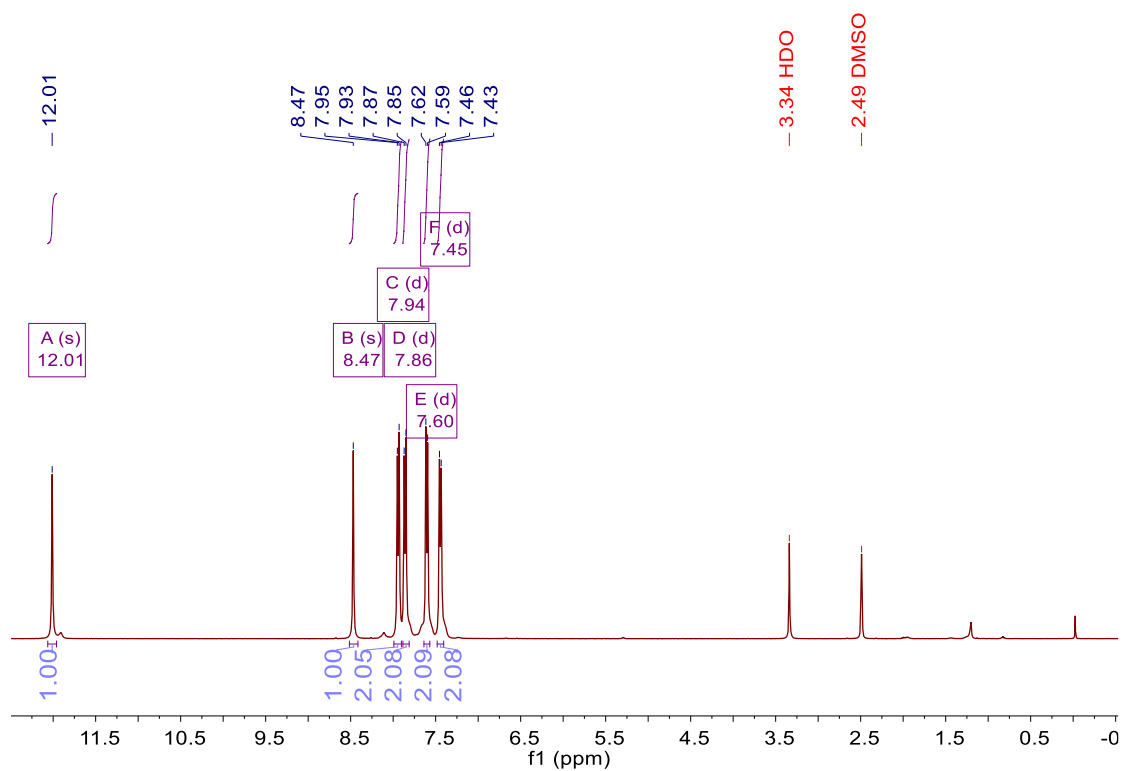
4. Supplementary Figures

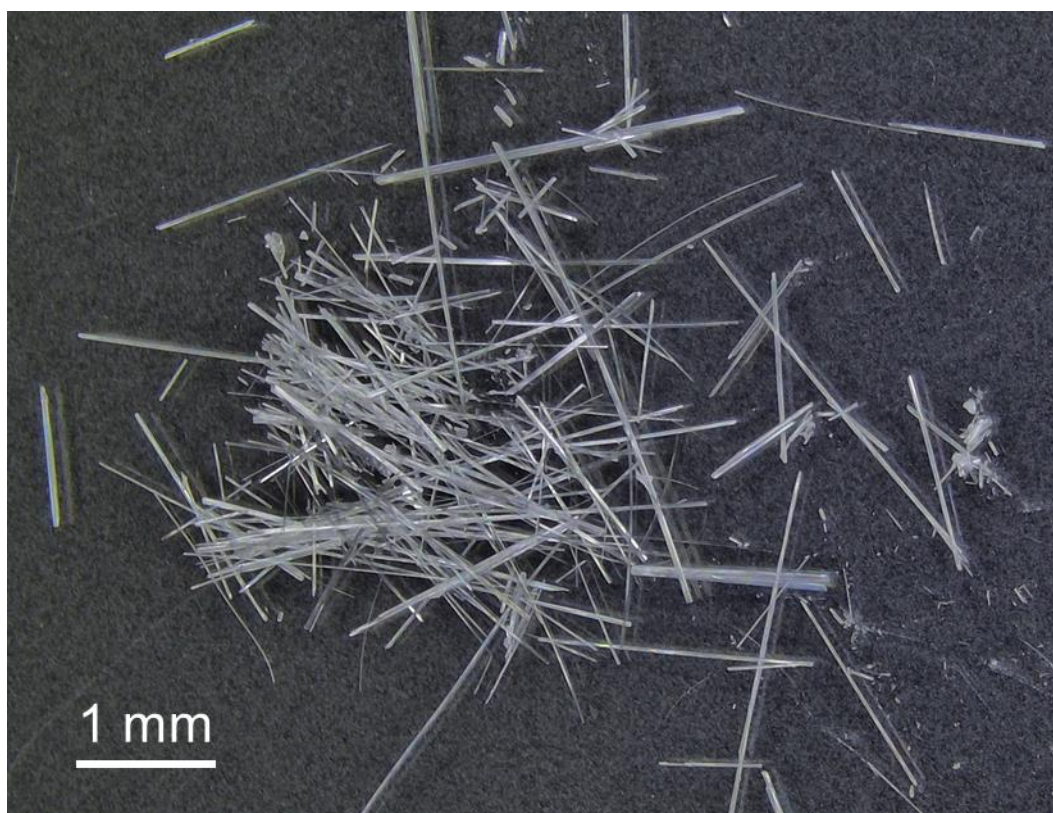**Fig. S1** ^{1}H NMR spectrum of CTBB in DMSO-d_6 (400 MHz).

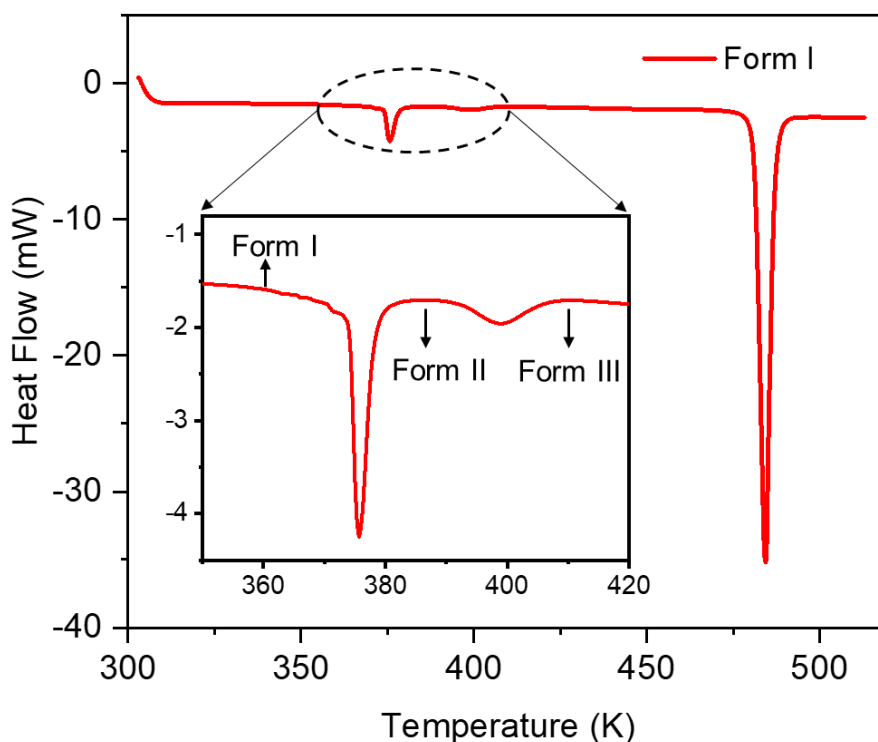**Fig. S2** Optical microscopic images of single crystals of form I.

Fig. S3 Differential Scanning Calorimetry (DSC) of microcrystals of form I. The curves show that there are three polymorphs, I, II and III, where form I undergoes a phase transition to form II at 374.3–385.8 K, and form II transforms to form III at 394.7–422.5 K.
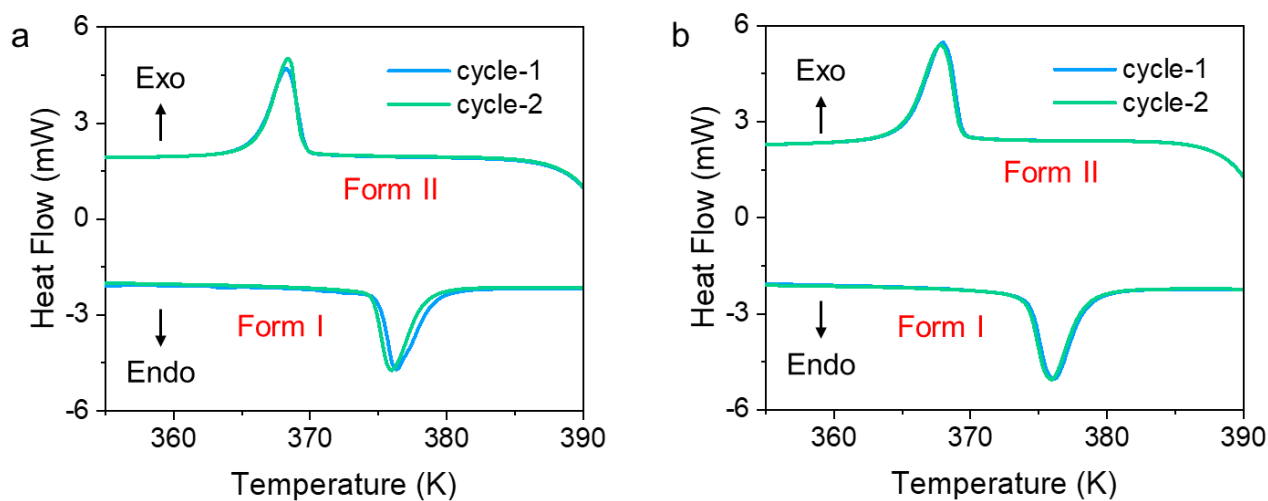

Fig. S4 Differential Scanning Calorimetry (DSC) of as-obtained (a) and lightly ground (b) crystals of Form I. (a) DSC profile recorded over two consecutive thermal cycles. Note the slight offset in the transition temperatures between the consecutive cycles. (b) Two thermal cycles in the DSC of lightly grinded crystals. The heating and cooling rates in all experiments were 10 K min^{-1}.
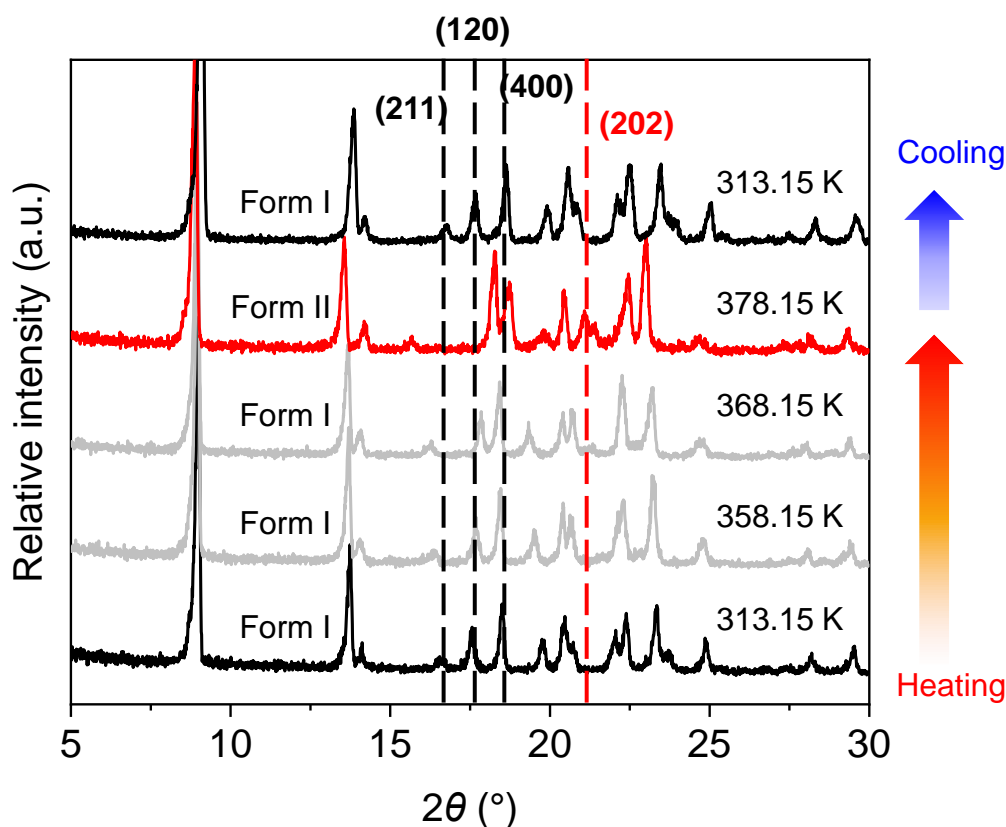
Fig. S5 Variable temperature PXRD of form I to form II. When the crystal was heated to 378.15 K, the characteristic peaks of (211), (120) and (400) of form I were obviously shifted, and the new peak of (202) of form II appeared. After the temperature cooling down to room temperature, the diffraction pattern could also return to the initial state. Therefore, it indicates that the phase transition from form I to form II is reversible.
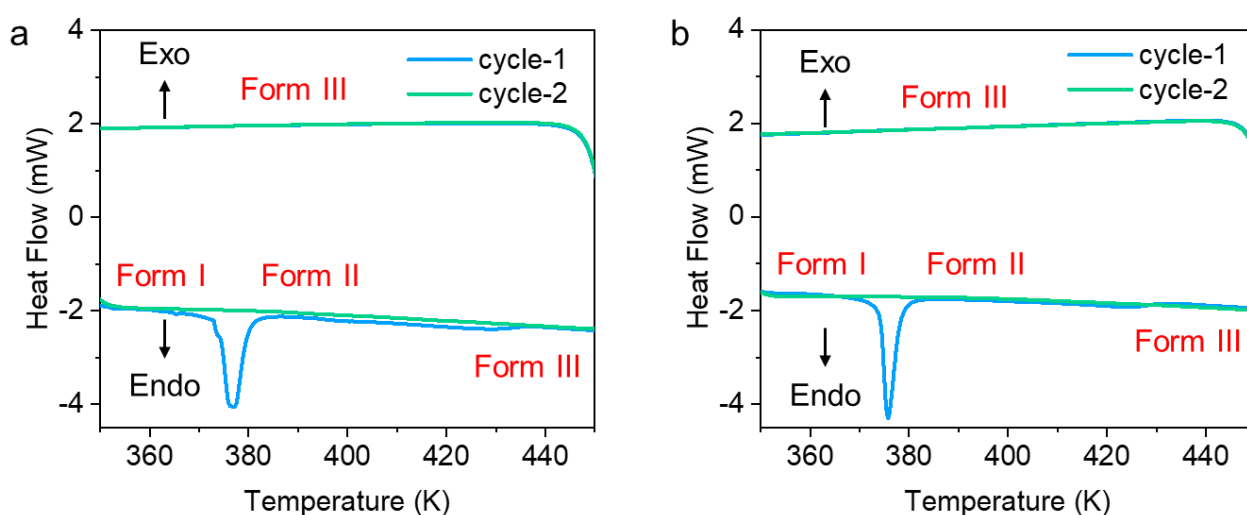

Fig. S6 Differential Scanning Calorimetry (DSC) of as-obtained (a) and lightly grinded (b) crystals of form I. The phase transition from form II to form III is irreversible. The heating and cooling rates in all experiments were 10 K min^{-1}.
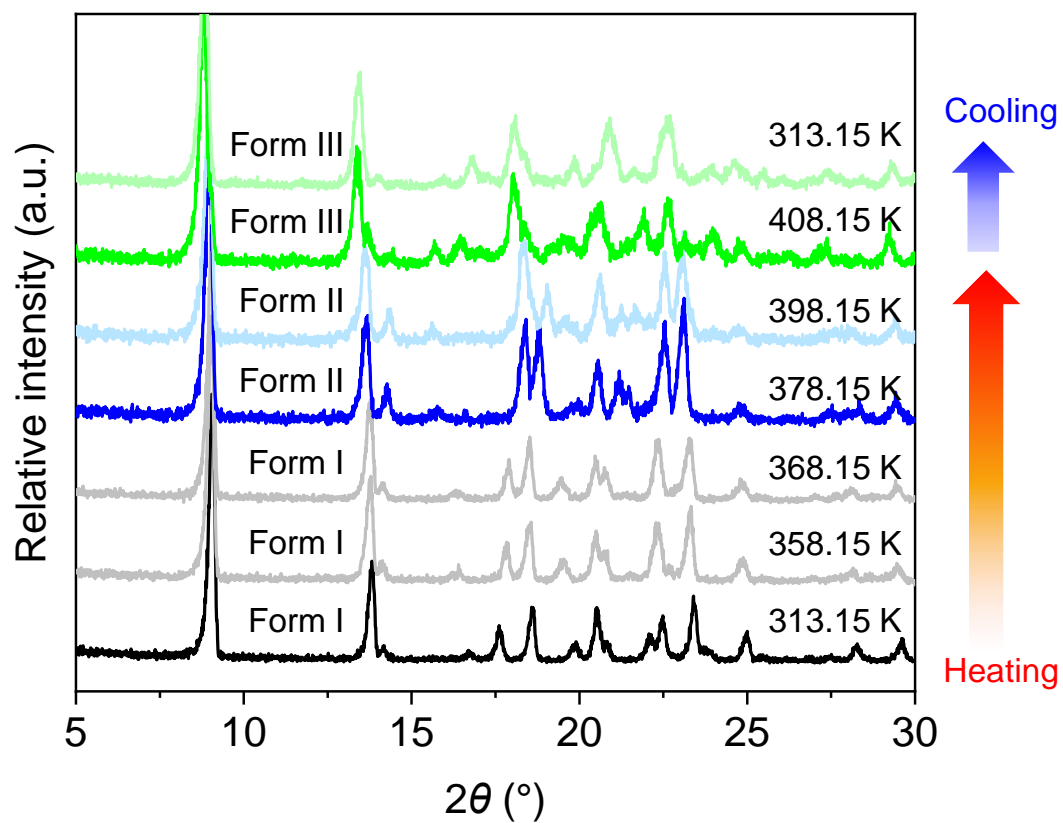
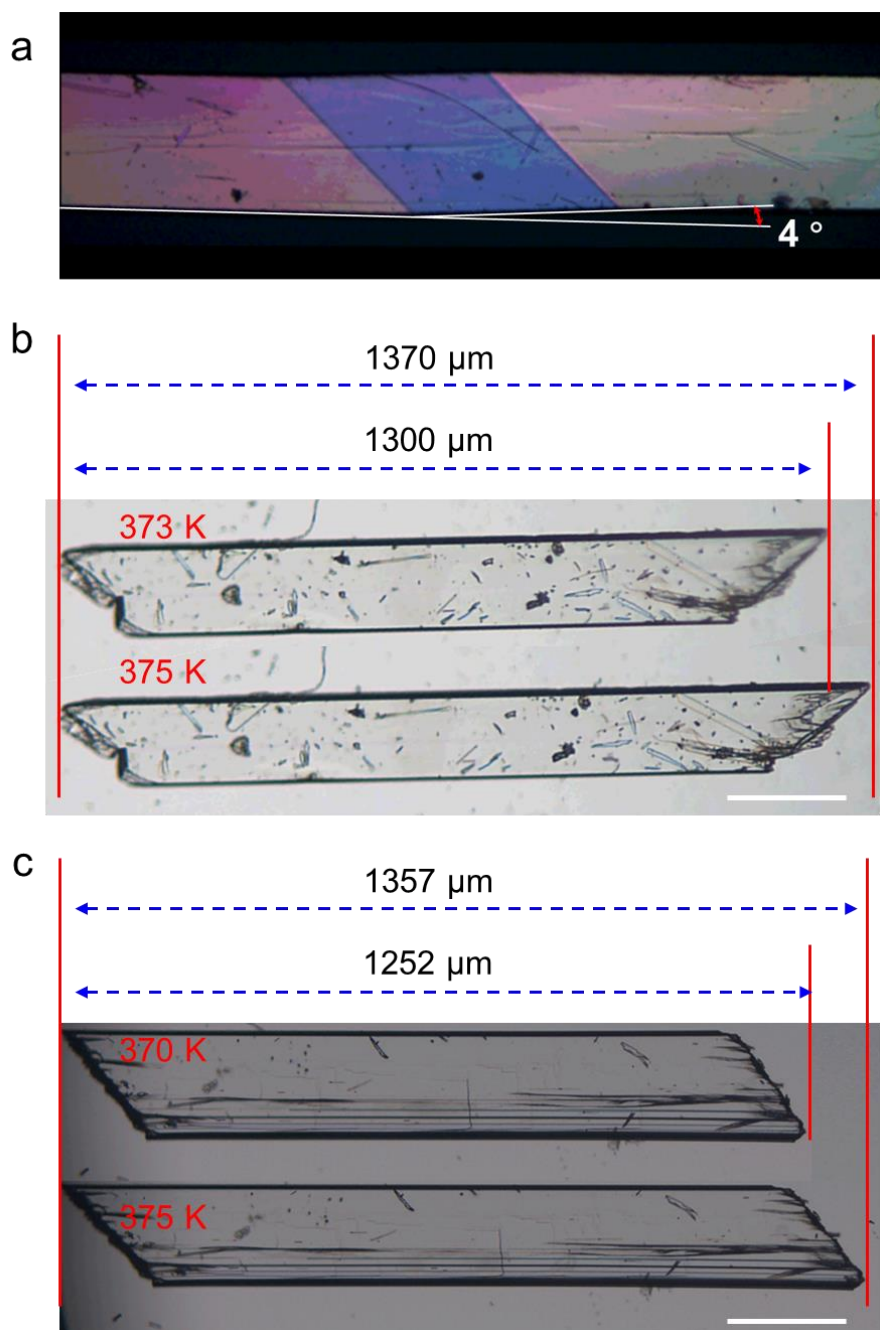**Fig. S7** Variable temperature PXRD of CTBB crystal at different temperatures.

Fig. S8 (a) The shear deformation of crystal during phase transition. (b, c) The elongation of different crystals. Scale bar 200 μm.
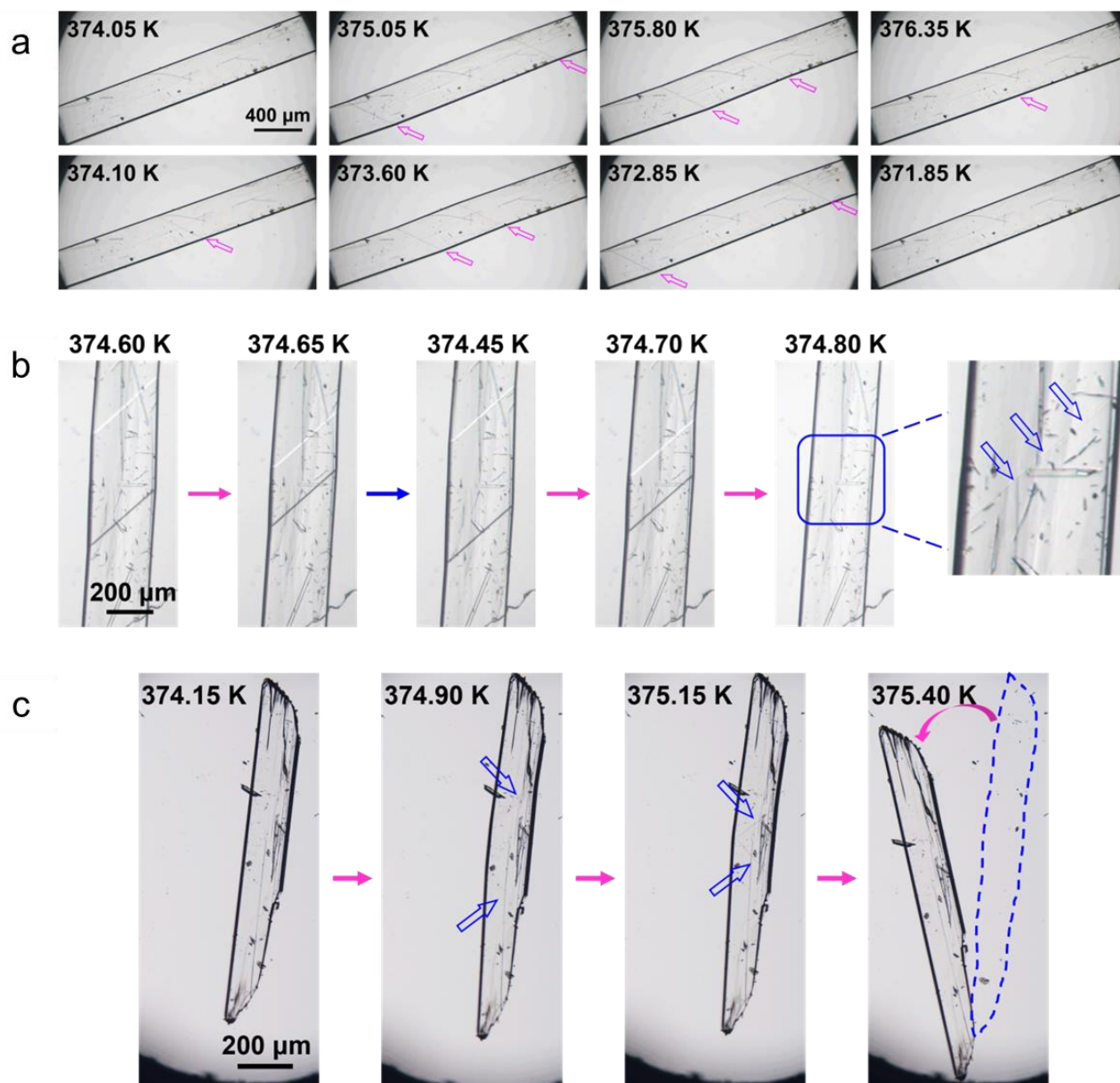
Fig. S9 (a) Progression of the phase transition observed by the migration of parallel phase boundaries induced by temperature variation at a rate of 5 K min^{-1}. (b) The reversible migration of paralleled phase boundaries by a control of the temperature variation at a rate of 1 K min^{-1}. (c) Thermosalient effects of a crystal during a phase transition that occurs by migration of non-parallel phase boundaries induced by heating at a rate of 10 K min^{-1}.
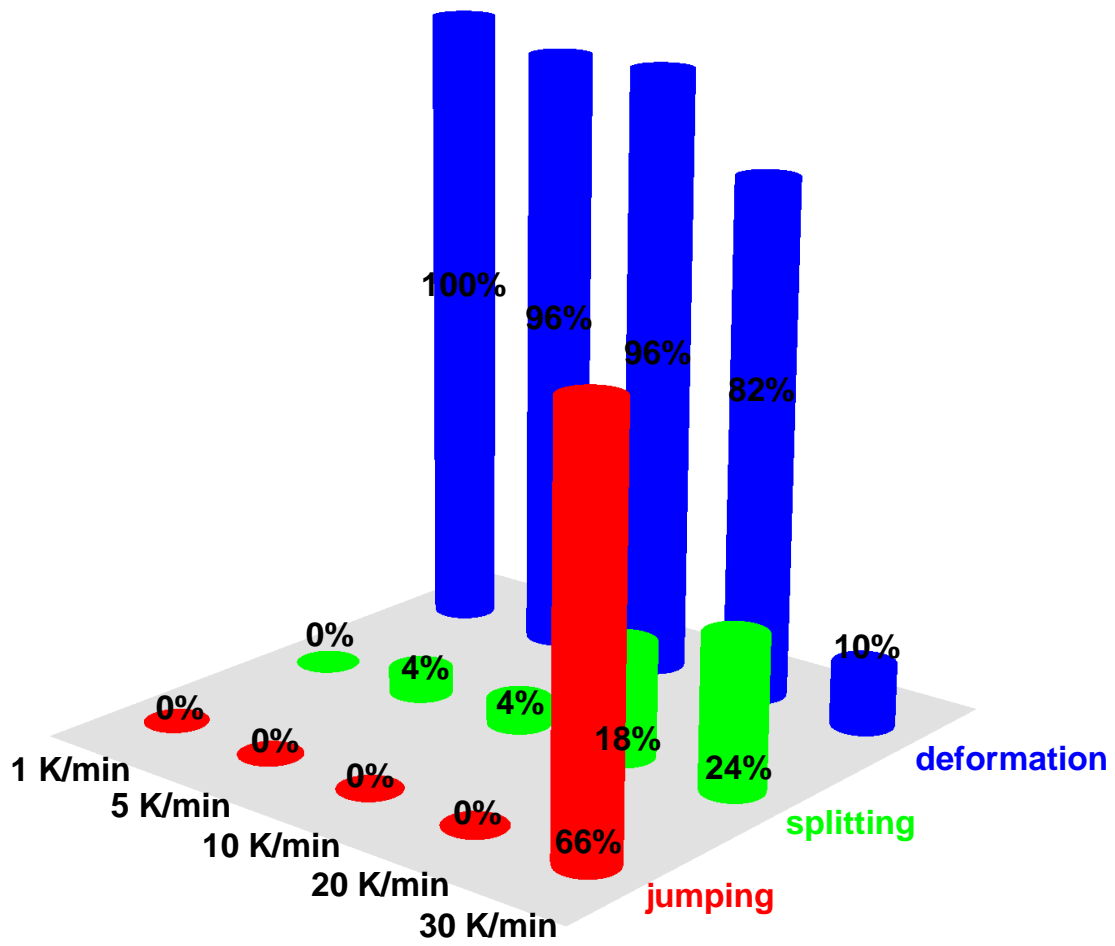
Fig. S10 Distribution of kinematic effects of the paralleled phase boundaries of CTBB crystals depending on the temperature variation rate.
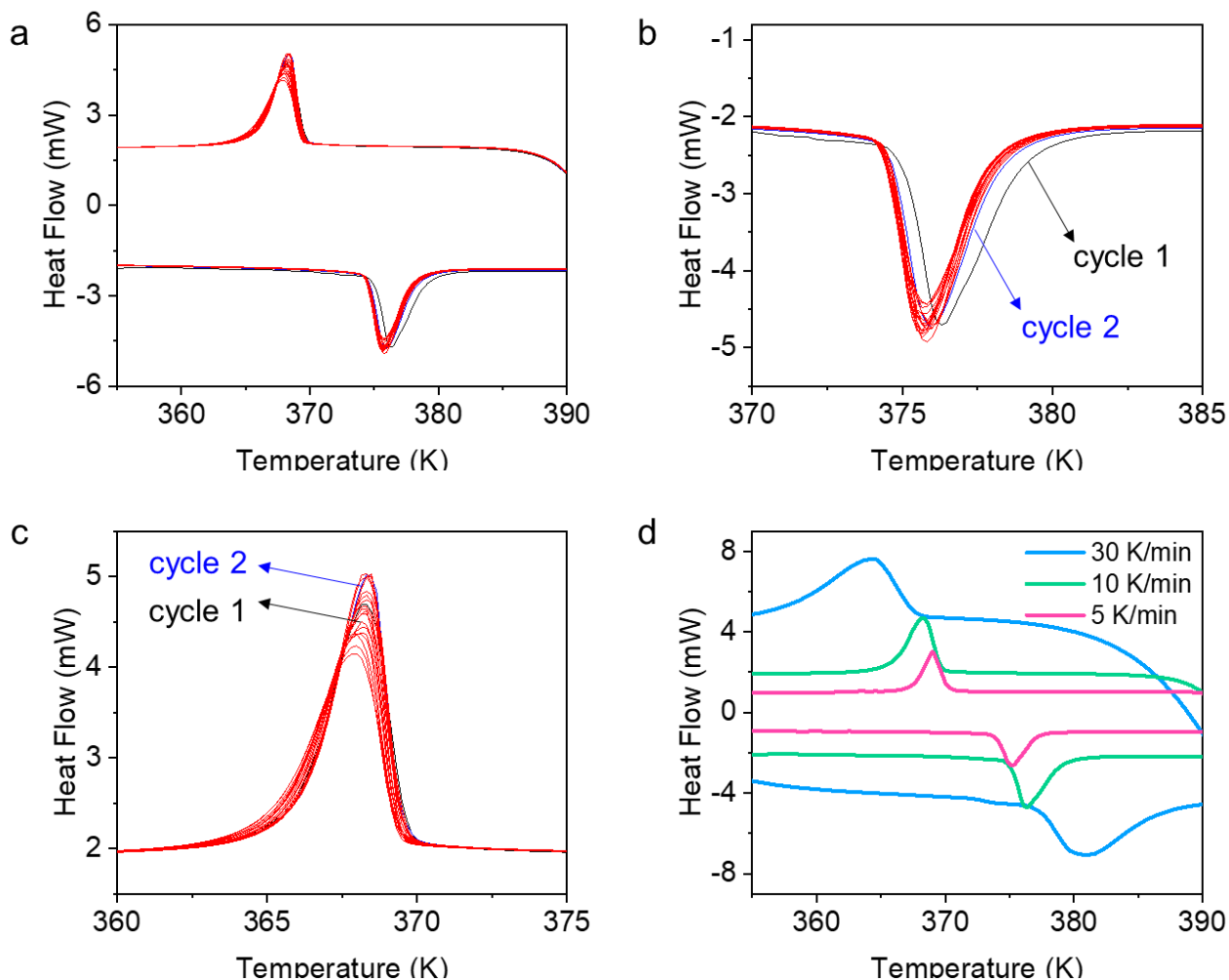
Fig. S11(a–c) Differential Scanning Calorimetry (DSC) of CTBB single crystals recorded over twenty consecutive thermal cycles. The heating and cooling rates were 10 K min^{-1}. (d) Effect of heating rate during heating and cooling cycles. Single crystals or lightly grinded crystals could be cycled between the two polymorphs by repeated heating and cooling with a small shift in the transition temperature between the first and the second thermal cycle. Faster heating/cooling rates delayed the first phase transition.
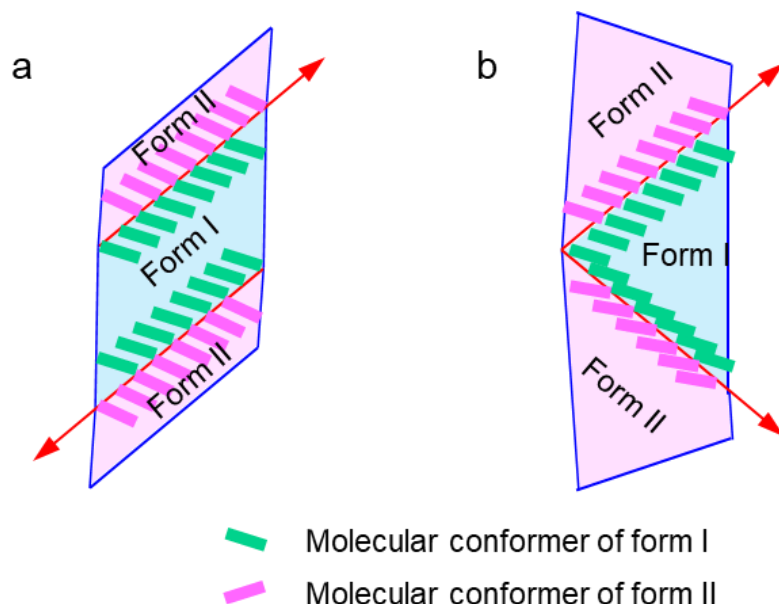
Fig. S12 Schematic illustration of the molecular arrangement on the (010) plane and its changes during the phase transition with different directions of the two phase boundaries. (a) When the parallel phase boundaries meet, the relationships between the two phases across the two boundaries are identical, and the two advancing phase fronts do not interfere with each other. (b) when the non-parallel phase boundaries meet, the junction leaves a large area where crystal remains untransformed. Additional energy is required to be absorbed and accumulated, which is finally released and converted into force that propels the crystal.
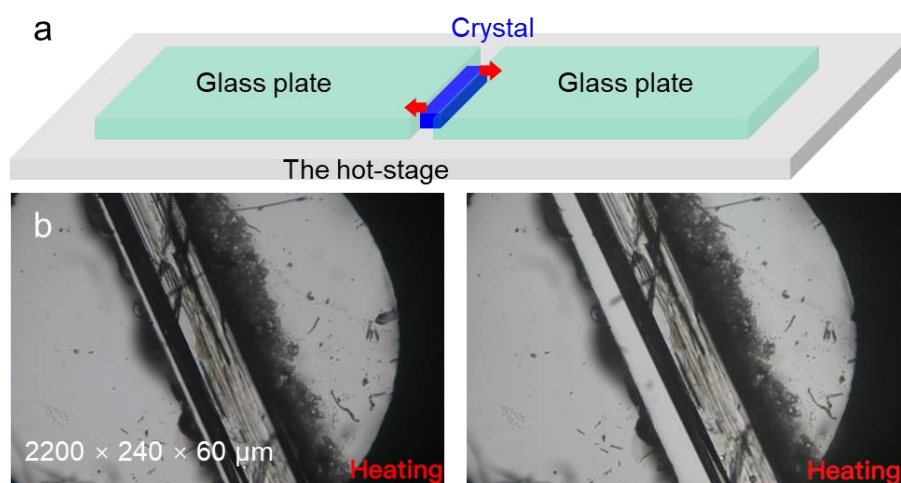

Fig. S13 The maximum pushing force of the crystals was tested by positioning a crystal between two parallel glass plates. (a) A crystal was placed between the plates on a flat substrate. The glass plates were moved apart by the crystal at the phase transition temperature, and the maximum pushing force was estimated by accounting for the maximum static friction between the glass plates and the glass substrate. The arrows show the direction of thermally induced crystal shear. (b) Each glass plate weighs 125 mg, and is $\sim2.6\times10^3$ times heavier than the crystal ($2,200 \times 240 \times 60$ μm). The glass plates were pushed apart by the crystal during the shape deformation and the crystal did not crack of was destroyed. The generated force was found to be about 1.1025×10^{-3} N, corresponding to 10^3 times its gravitational force. The photos were extracted from Supplementary Movie 10.
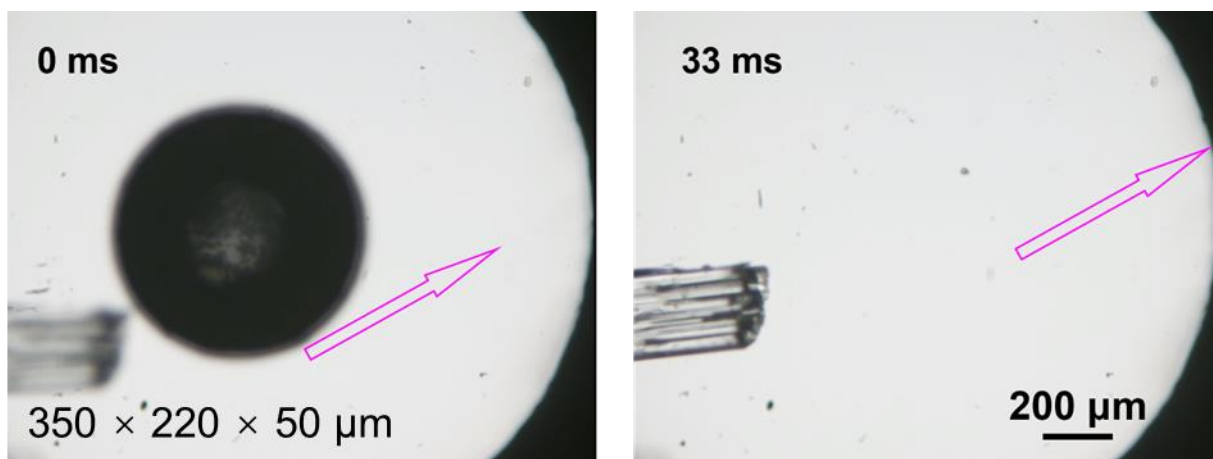
Fig. S14 Displacement of an object (abead) by crystal deformation. The work generated by the sudden elongation of the fixed crystal was evaluated by the displacement of a 1.12 mg iron bead. The pink arrows mark the position of the bead at 0 ms, and the direction of the bead movement at 33 and 66 ms, respectively. The photos were extracted from Supplementary Movie 11.
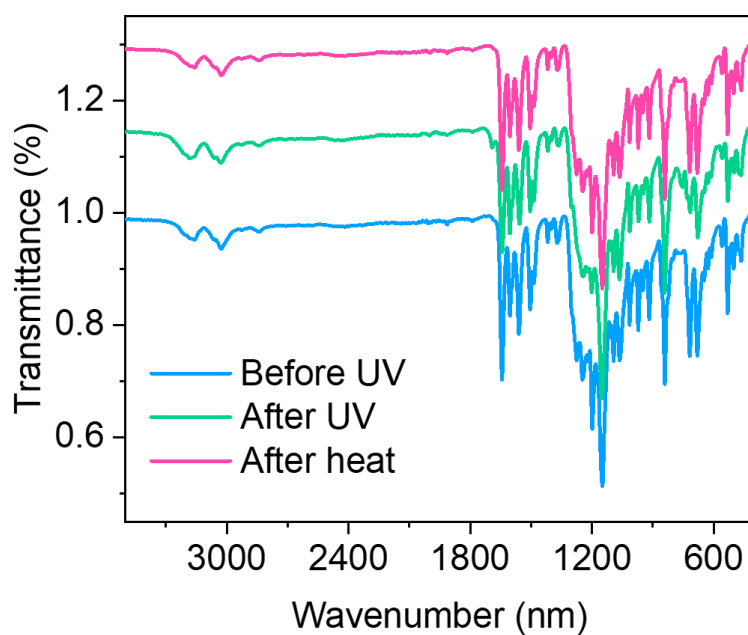
Fig. S15 Infrared spectra of CTBB microcrystals in form I before and after irradiation by a 365 nm light for 5 minutes, and after heating at 374 K for 5 minutes.
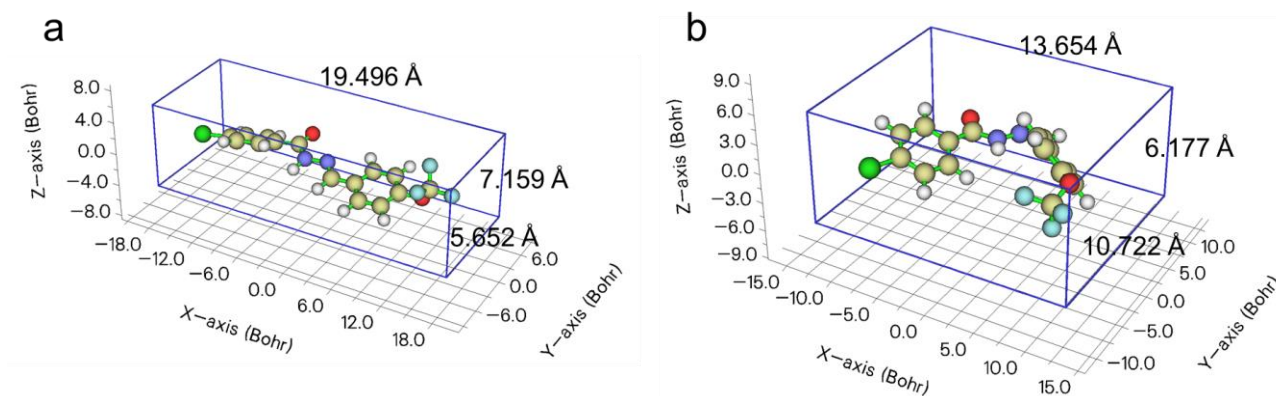
Fig. S16 Geometric optimization and change in shape of a molecule of (a) *trans-* and (b) *cis-*CTBB in the gas phase. After photoisomerization, the length, thickness, and width of *trans-*CTBB changed by –29.97% (–5.842 Å), –13.72% (–0.982 Å), and +89.70% (+5.070 Å), respectively.
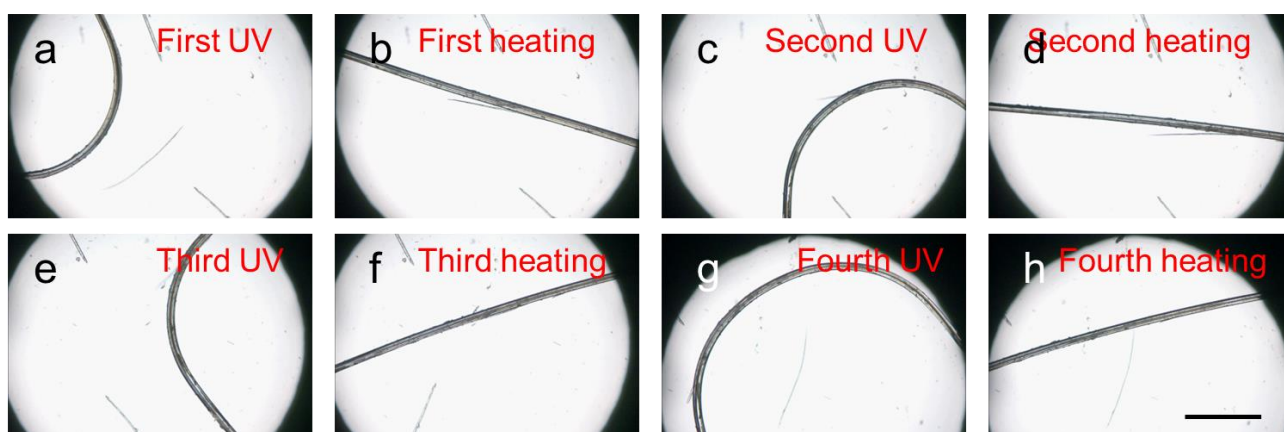
Fig. S17 (a–h) Four cycles of crystal bending by ultraviolet irradiation and straightening by heat. The length of the scale bar is 500 μm.
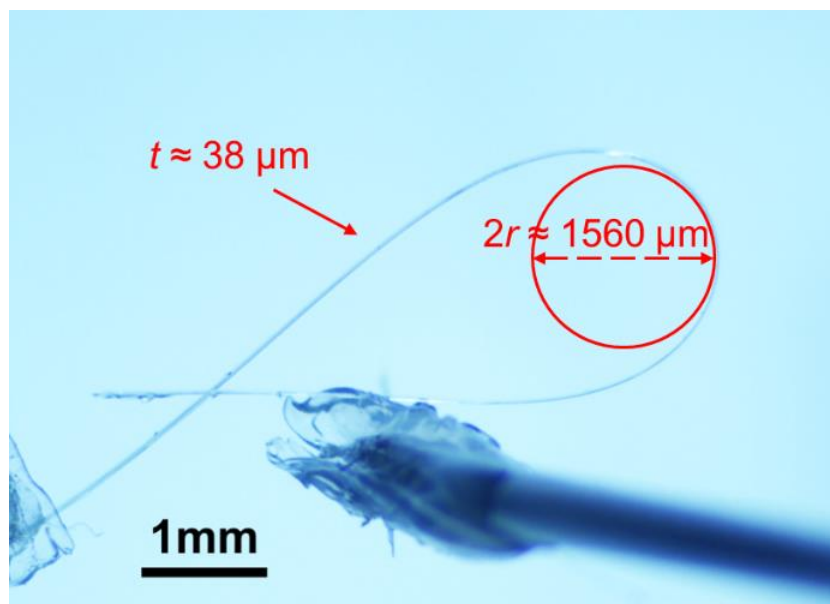
Max. elastic strain, $\varepsilon = t/2r = 2.4\%$
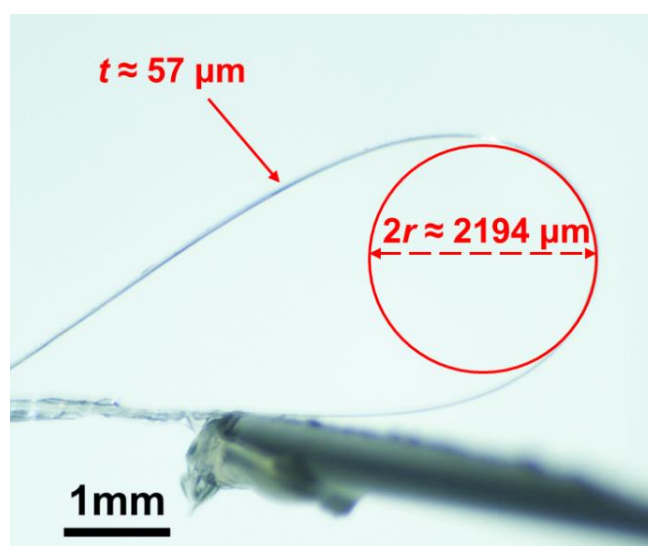
Max. elastic strain, $\varepsilon = t/2r = 2.6\%$

Fig. S18 Calculation of the elastic strain of CTBB crystals along the major face, (001).

Fig. S19 Experimental setups for measurement of the temperature flexibility (a), and elastic bending (b) of form II.
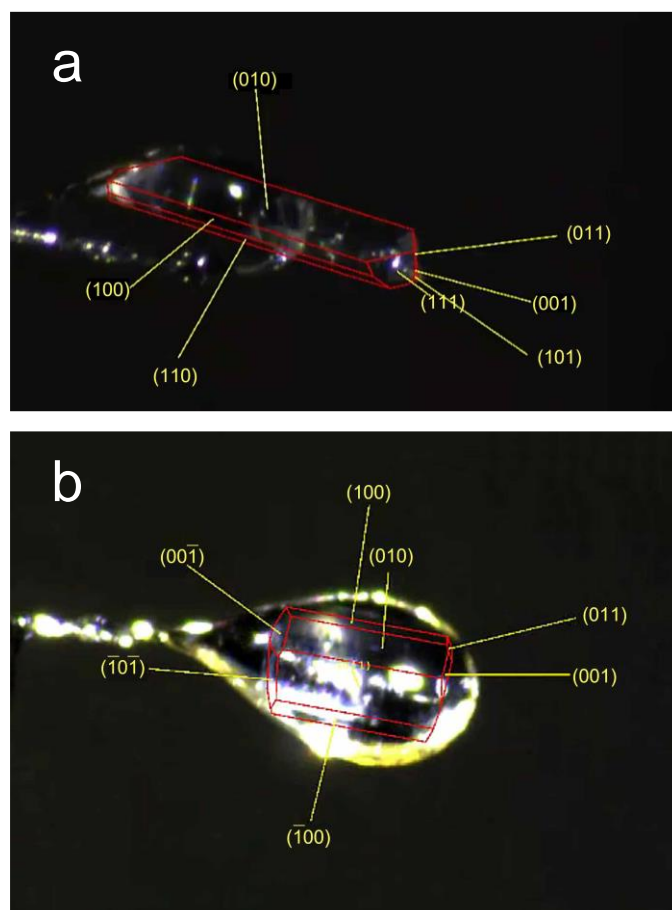
Fig. S20 Face indexing images of form I (a) and form II (b), respectively.

				Energy Framework of Form I		

	view along *a* axis	view along *b* axis	view along *c* axis
Total interaction energy			
Dispersion energy			
Electrostatic energy			
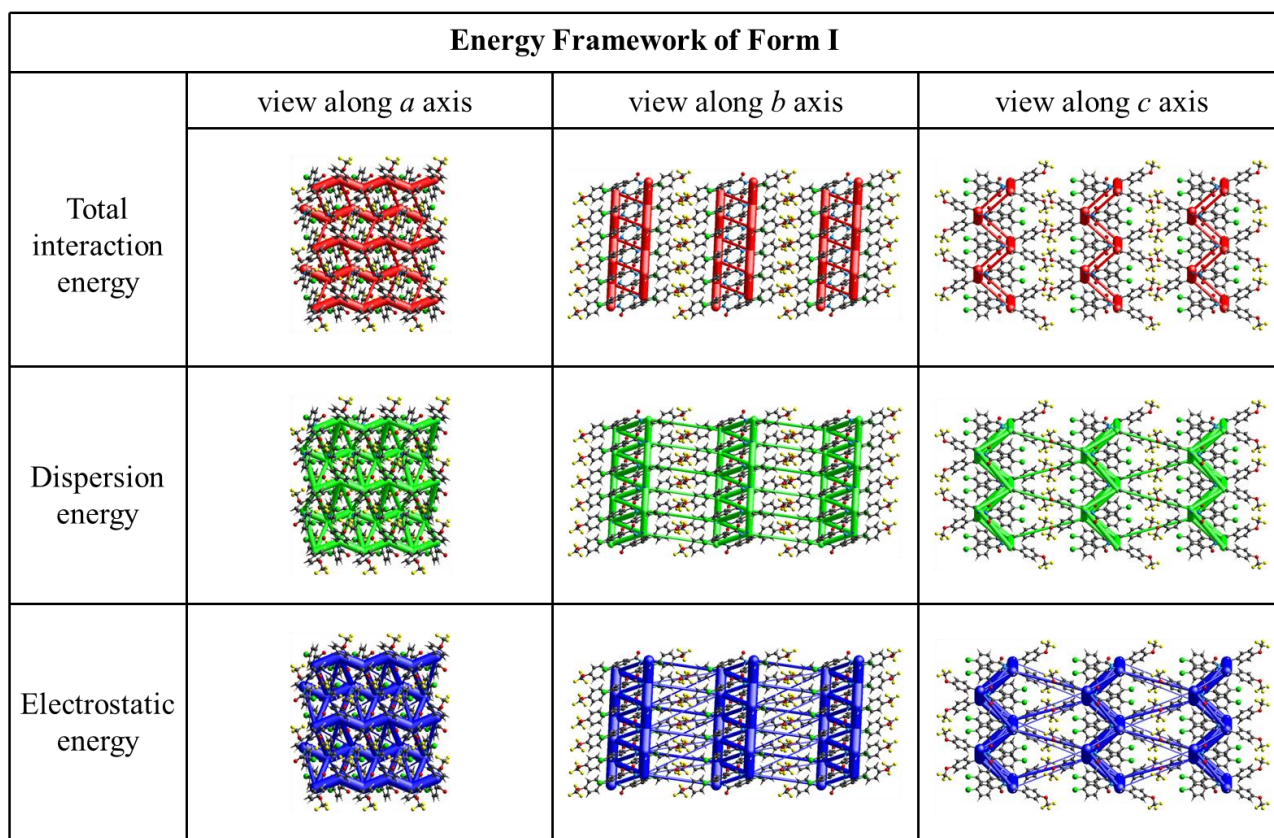
Fig. S21 Three-dimensional topologies of the energy framework for form I.

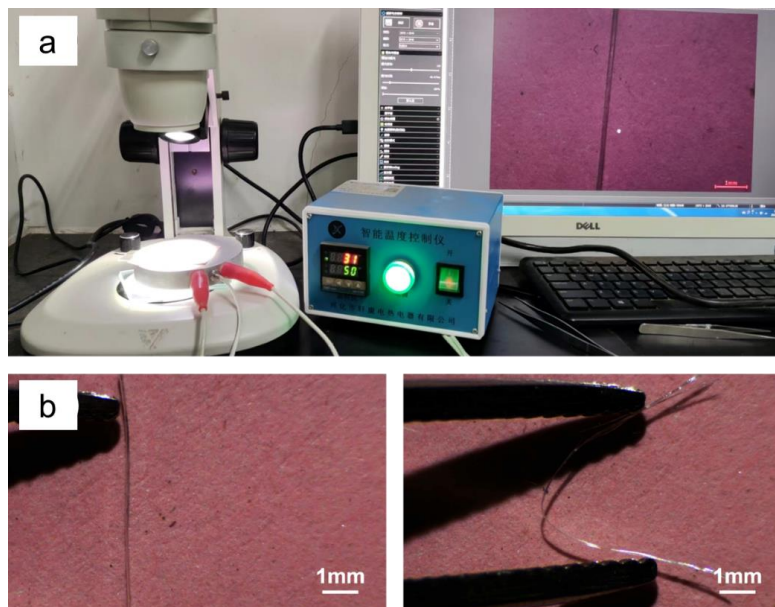|	N	Symop	R	Electron Density	E_ele	E_pol	E_dis	E_rep	E_tot
	2	-x, y+1/2, -z+1/2	8.02	B3LYP/6-31G(d, p)	-15.3	-3.3	-29.0	15.8	-34.0
	2	-x, -y+1/2, z+1/2	4.49	B3LYP/6-31G(d, p)	-52.3	-13.8	-49.7	71.0	-65.0
	1	-x, -y, -z	9.55	B3LYP/6-31G(d, p)	-1.0	-2.0	-36.5	17.5	-23.5
	1	-x, -y, -z	14.58	B3LYP/6-31G(d, p)	-1.9	-0.2	-9.0	2.0	-8.8
	2	x, -y+1/2, z+1/2	9.17	B3LYP/6-31G(d, p)	1.1	-0.2	-7.2	1.9	-4.1
	2	-x, y+1/2, -z+1/2	10.18	B3LYP/6-31G(d, p)	-1.5	-0.8	-6.6	5.3	-4.7
	1	-x, -y, -z	13.15	B3LYP/6-31G(d, p)	-3.4	-0.6	-17.7	4.5	-16.6
	2	-x, y+1/2, -z+1/2	13.87	B3LYP/6-31G(d, p)	-0.7	-0.1	-8.2	1.8	-6.9
	1	-x, -y, -z	7.18	B3LYP/6-31G(d, p)	5.0	-3.5	-29.6	14.0	-14.4
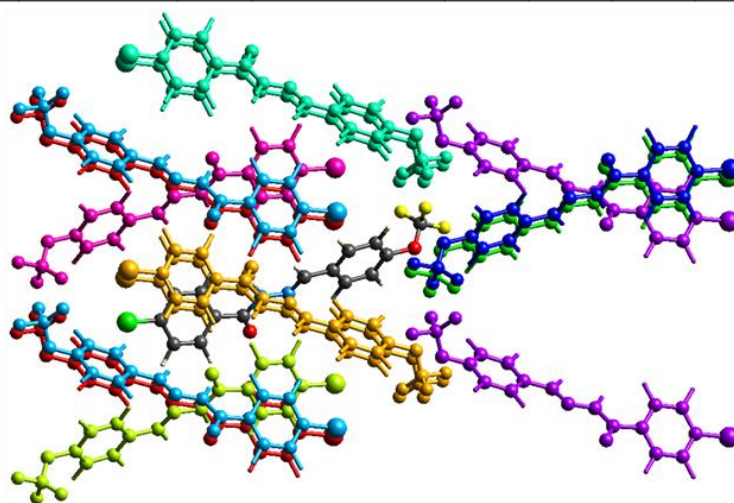
Fig. S22 Molecular pairs and interaction energies obtained from the energy frameworks for form I.
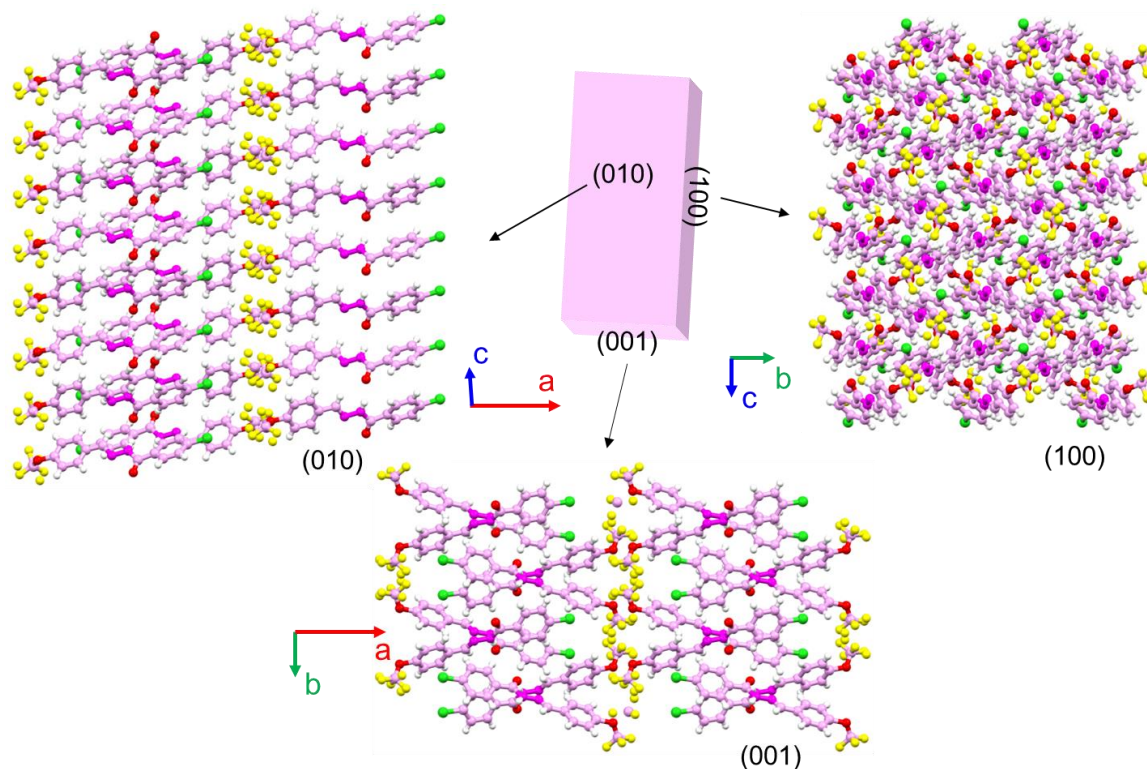
Fig. S23 Molecular packing in the structure of form II viewed perpendicular to the faces (001), (010), and (100) planes, respectively.

Energy Framework of Form II			
	view along *a* axis	view along *b* axis	view along *c* axis
Total interaction energy			
Dispersion energy			
Electrostatic energy			

Fig. S24 Three-dimensional topologies of the energy frameworks for form II.

|	N	Symop	R	Electron Density	E_ele	E_pol	E_dis	E_rep	E_tot
	1	-x, -y, -z	14.71	B3LYP/6-31G(d, p)	-1.2	-0.2	-6.5	1.0	-6.5
	2	-x, y+1/2, -z+1/2	14.05	B3LYP/6-31G(d, p)	-1.1	-0.3	-9.2	2.1	-8.1
	1	-x, -y, -z	13.78	B3LYP/6-31G(d, p)	-0.7	-0.5	-9.8	0.8	-9.2
	2	x, -y+1/2, z+1/2	8.96	B3LYP/6-31G(d, p)	1.0	-0.3	-6.4	1.5	-3.8
	2	-x, y+1/2, -z+1/2	8.04	B3LYP/6-31G(d, p)	-11.1	-2.3	-24.6	11.3	-27.8
	2	x, -y+1/2, z+1/2	4.74	B3LYP/6-31G(d, p)	-49.1	-12.8	-40.7	63.3	-57.7
	1	-x, -y, -z	8.92	B3LYP/6-31G(d, p)	-0.7	-1.8	-41.4	17.8	-27.1
	2	-x, y+1/2, -z+1/2	9.70	B3LYP/6-31G(d, p)	-1.9	-0.9	-7.8	7.3	-5.0
	1	-x, -y, -z	6.81	B3LYP/6-31G(d, p)	-0.3	-3.2	-31.8	10.7	-23.8
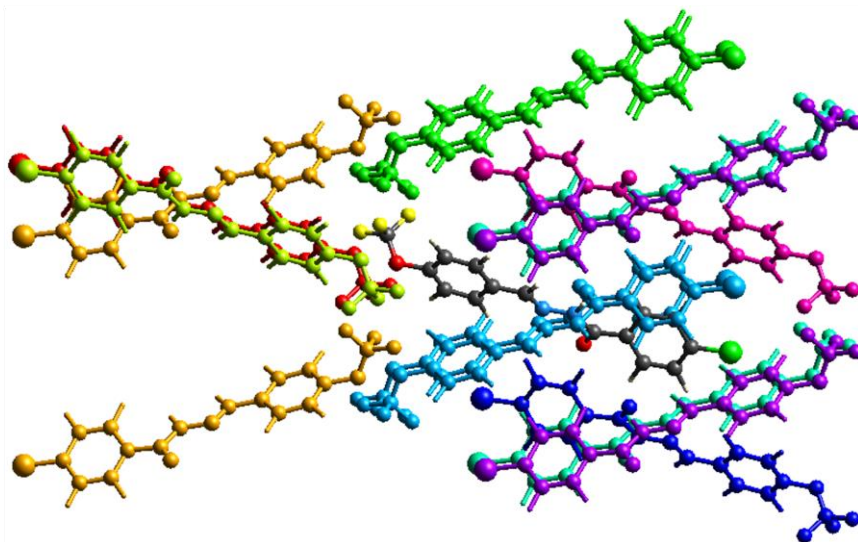
Fig. S25 Molecular pairs and interaction energies obtained from the energy frameworks for form II.
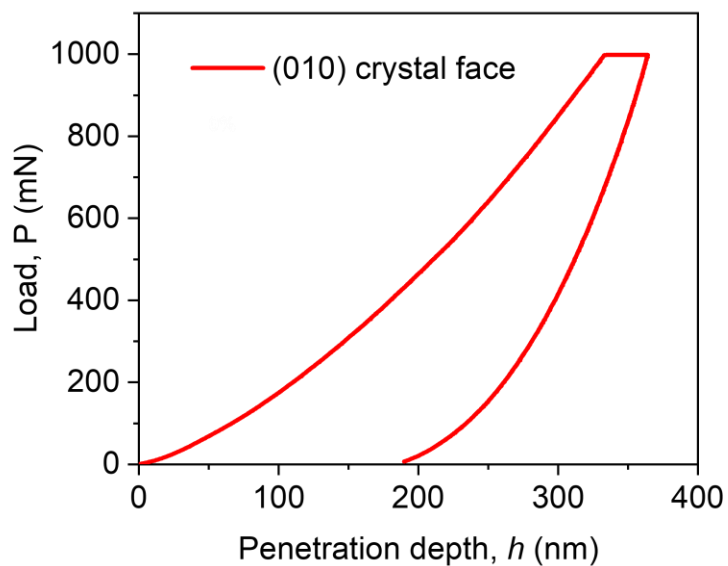

Fig. S26 Load-displacement curves of CTBB crystals obtained by nanoindentation on the (010) face of form I.

Supplementary Tables

Table S1. Crystallographic data and refinement details for CTBB

	Form I	**Form I**	**Form I**	**Form II**	**Form II**	**Form III**
Temperature / K	113.15	298	365	374.4	380	113.15
Formula weight	342.7	342.7	342.7	342.7	342.7	342.7
Crystal system	monoclinic	Monoclinic	monoclinic	monoclinic	monoclinic	monoclinic
Space group	$P2_1/c$	$P2_1/c$	$P2_1/c$	$P2_1/c$	$P2_1/c$	$P2_1/c$
a / Å	18.5603(2)	18.6718(16)	18.847(6)	19.0164(19)	19.031(16)	19.074(6)
b / Å	10.25450(10)	10.1775(10)	10.089(3)	9.4918(12)	9.539(8)	9.480(3)
c / Å	7.79550(10)	8.0982(8)	8.313(2)	8.9166(11)	8.813(7)	8.983(3)
α / °	90	90	90	90	90	90
β / °	94.450(10)	92.583(3)	90.989(10)	85.985(10)	86.26(3)	94.741(10)
γ / °	90	90	90	90	90	90
Volume / Å^3	1479.22(3)	1537.4(3)	1580.4(8)	1605.5(3)	1596(2)	1618.7(9)
Z	4	4	4	4	4	4
Density / (g cm^{-3})	1.539	1.481	1.44	1.426	1.426	1.406
F_{000}	696	696	696	696	696	696
h_{min}, h_{max}	–23, 23	–24, 24	–24, 21	–22, 23	–24, 24	–22, 22
k_{min}, k_{max}	–12, 12	–13, 12	–13, 12	–10, 11	–9, 12	–10, 11
l_{min}, l_{max}	–9, 7	–10, 10	–10, 10	–10, 9	–11, 11	–10, 10
No. of measured reflections	2841	2635	1857	2942	1115	1090
No. of unique reflections	237	245	246	208	245	208
No. of reflections used	96	127	145	2364	182	31
R_{all}, R_{obs}	0.0427, 0.0385	0.0871, 0.055	0.1582, 0.0677	0.0956 0.0801	0.2947, 0.1226	0.2174, 0.1007
$wR_{2,all}$, $wR_{2,obs}$	0.1093, 0.1052	0.1364, 0.1189	0.1986, 0.1518	0.3238 0.2936	0.3455, 0.2577	0.3280, 0.2685
$\Delta\rho_{min,max}$ / (e Å^{-3})	–0.391, 0.333	–0.368, 0.253	–0.213, 0.236	0.3238 0.295	–0.162, 0.16	–0.218, 0.303
GooF	1.084	1.027	1.021	1.210	1.006	1.196
CCDC No.	2286243	2286247	2286249	2341752	2286528	2286530

Table S2. Temperatures and thermal hysteresis widths between the forward (heating) and backward (cooling) phase transition of some thermosalient crystals

Crystal	Forward transition temperature	Backward transition temperature	Temperature hysteresis width	Reference
Terephthalic acid	348–458 K	305–315 K	43 K	[4]
(Phenylazophenyl)palladiumhexa-fluoroacetylacetonate	69.1–76.9 °C	32.1–52.7 °C	24.2 °C	[5]
6-Chloronicotinic acid	388.15–395.15 K	365.15–373.15 K	22 K	[6]
Guanidinium nitrate	295–305 K	265–275 K	30 K	[7]
2,7-di([1,1′-biphenyl]-4-yl)-fluorenone	parallel phase boundaries		2-3 K	[8]
	single or non-parallel phase boundaries		≈18 K	

Table S3. Variation of unit cell lattice parameter from 298 K to 388 K.

Temperature	a / Å	b / Å	c / Å	β / °	V / Å^3
298.0	18.6718	10.1775	8.0982	92.583	1537.40
300.8	18.6842	10.1868	8.1107	92.496	1542.26
308.0	18.6933	10.1828	8.1233	92.407	1544.91
318.0	18.7084	10.1701	8.1497	92.207	1549.46
328.0	18.7183	10.1540	8.1880	91.958	1555.35
338.0	18.7371	10.1358	8.2260	91.691	1561.56
348.0	18.7500	10.1109	8.2672	91.396	1566.83
358.0	18.7720	10.0743	8.3219	90.975	1573.57
368.0	18.7826	10.0129	8.4064	90.397	1580.94
374.4	19.0164	9.4918	8.9166	85.985	1605.50
378.0	19.0480	9.4658	8.9140	85.613	1602.53
388.0	19.0520	9.4300	9.0074	84.939	1612.00

Supplementary References

[1]   G. Sheldrick, *Acta crystallographica. Section A* **2015**, *71*, 3-8.

[2]   C. B. Hubschle, G. M. Sheldrick, B. Dittrich, *J. Appl. Crystallogr.* **2011**, *44*, 1281-1284.

[3]   M. J. Turner, S. P. Thomas, M. W. Shi, D. Jayatilaka, M. A. Spackman, *ChemComm* **2015**, *51*, 3735-3738.

[4]   D. P. Karothu, J. Weston, I. T. Desta, P. Naumov, *J. Am. Chem. Soc.* **2016**, *138*, 13298-13306.

[5]   S. C. Sahoo, M. K. Panda, N. K. Nath, P. Naumov, *J. Am. Chem. Soc.* **2013**, *135*, 12241-12251.

[6]   J. Lin, Z. Guo, K. Zhang, P. Zhao, S. Wu, J. Xu, J. Gong, Y. Bao, *Adv. Funct. Mater.* **2022**, *32*, 2203004.

[7]   D. P. Karothu, R. Ferreira, G. Dushaq, E. Ahmed, L. Catalano, J. M. Halabi, Z. Alhaddad, I. Tahir, L. Li, S. Mohamed, M. Rasras, P. Naumov, *Nat. Commun.* **2022**, *13*, 2823.

[8]   Y. Duan, S. Semin, P. Tinnemans, J. Xu, T. Rasing, *Small* **2021**, *17*, 2006757.